ELSEVIER

Volume 181, Number 11, November 2008

JOURNAL OF SOLID STATE CHEMISTRY

www.elsevier.com/locate/jssc

# CONTENTS

Abstracted/indexed in BioEngineering Abstracts, Chemical Abstracts, Coal Abstracts, Current Contents/Physics, Chemical, & Earth Sciences, Engineering Index, Research Alert, SCISEARCH, Science Abstracts, and Science Citation Index. Also covered in the abstract and citation database SCOPUS®. Full text available on ScienceDirect®.

## *Regular Articles*



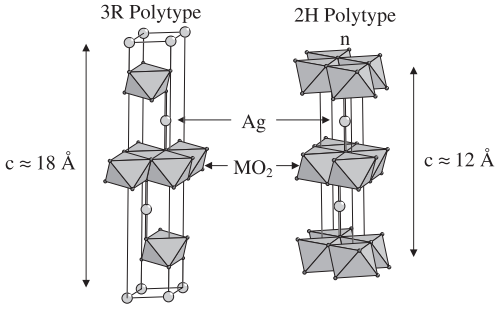


Comparison of the structures of high-temperature $AgCoO_2$ (left, 3R structure) and of new $AgCoO_{2+\partial}$(IE) (right, 6H structure). The latter is obtained topotactically from $Na_{0.7}CoO_2$ by ion exchange in molten nitrates. Detailed studies showed that $AgCoO_{2+\partial}$(IE) is slightly over-stoichiometric in oxygen ($\partial = 0.06$).



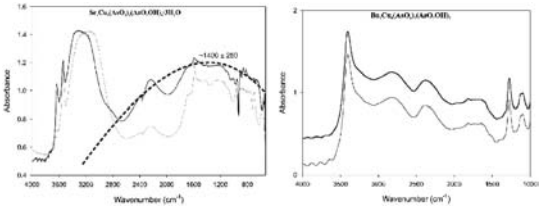

The two new compounds, $Sr_4Cu_3(AsO_4)_2(AsO_3OH)_4 \cdot 3H_2O$ **(1)** and $Ba_2Cu_4(AsO_4)_2(AsO_3OH)_3$ **(2)**, were synthesized under hydrothermal conditions. They represent previously unknown structure types and are the first compounds synthesized in the systems SrO/BaO–CuO–$As_2O_5$–$H_2O$. Their crystal structures were determined by single-crystal X-ray diffraction [space group $C2/c$, $a = 18.536(4)$ Å, $b = 5.179(1)$ Å, $c = 24.898(5)$ Å, $\beta = 93.67(3)^\circ$, $V = 2344.0(8)$ Å$^3$, $Z = 4$ for **1**; space group $P4_2/n$, $a = 7.775(1)$ Å, $c = 13.698(3)$ Å, $V = 828.1(2)$ Å$^3$, $Z = 2$ for **2**]. Vibrational spectra (FTIR and Raman) of both compounds are described. The spectroscopic manifestation of the very short hydrogen bond, where the donor and acceptor are crystallographically different in **1**, and ABC-like spectra in **2** were discussed.

## *Regular Articles—Continued*



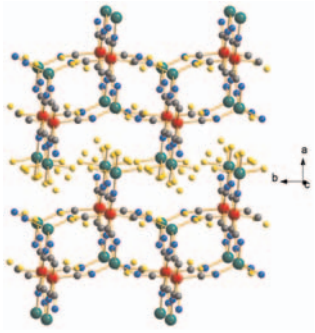

Structure of stacked layers for $CO_2[Fe(CN)_6] \cdot xH_2O$.



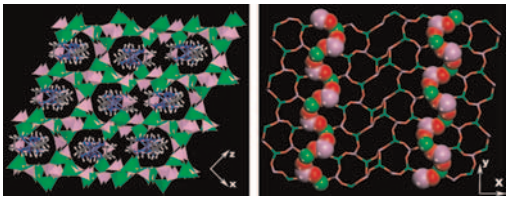

A new three-dimensional zincophosphite containing left-handed and right-handed helical chains has been solvothermally synthesized using $Co(en)_3Cl_3$ as the structure-directing agent.

*Continued*

**High-pressure single-crystal X-ray diffraction of $Tl_2SeO_4$**
Andrzej Grzechnik, Tomasz Breczewski and Karen Friese
***Page 2914***

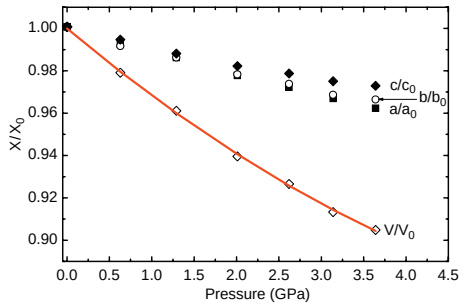


Pressure dependence of normalized lattice parameters and unit-cell volumes in $Tl_2SeO_4$ (*Pmcn*, $Z=4$). The solid line is the Murnaghan equation of state.

---

**Uncontrollable expansion of $PbZn_{1/3}Nb_{2/3}O_3$–$PbTiO_3$ perovskite ⇒ pyrochlore transition during spark plasma sintering: Mechanism proposal using infinite periodic minimal surfaces**
T. Hungria, A. Castro, M. Alguero and J. Galy
***Page 2918***

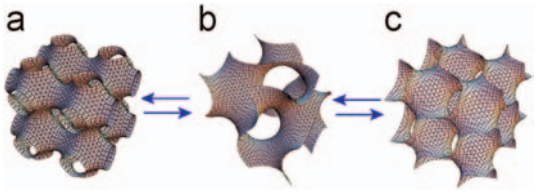


The explosive phenomenon observed during the sintering of PZN–PT phase using spark plasma sintering is directly linked to the perovskite ⇒ pyrochlore phase transition and the volume increase related to the role of the Pb lone pairs. Infinite periodic minimal surfaces have been used to describe the structures and the phase transition.

---

**Synthesis and characterisation of a novel europium-based graphite intercalation compound**
Nicolas Emery, Claire Hérold, Christine Bellouard, Pierre Delcroix, Jean-François Marêché and Philippe Lagrange
***Page 2924***

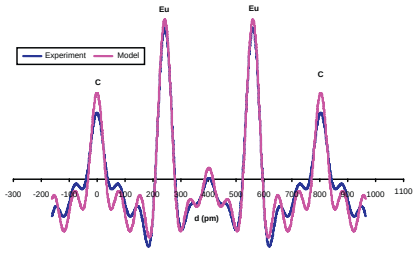


1D electronic density profiles along the *c*-axis of $Li_xEuC_4$.

**$Sr_4AlNbO_8$: A new crystal structure type determined from powder X-ray data**
Eungje Lee and Seung-Tae Hong
***Page 2930***

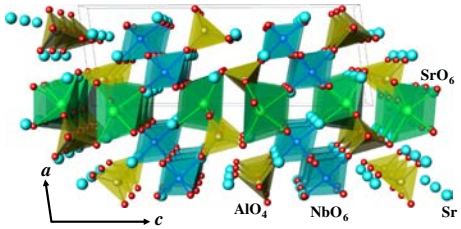


The crystal structure type of $Sr_4AlNbO_8$ is new, and may be described as a three-dimensional polyhedral network resulting from the corner-sharing of $NbO_6$ and $Sr1O_6$ octahedra and $AlO_4$ tetrahedra. Also, the other strontium atoms (Sr2, Sr3, and Sr4) occupy the larger cavities surrounded by oxygen atoms.

---

**In-situ carboxylation and synthesis of two novel Sm(III) coordination polymers assembled from 5-hydroxyisophthalate and nitrate, chloride in hydrothermal reaction**
Yan Huang, Bing Yan and Min Shao
***Page 2935***

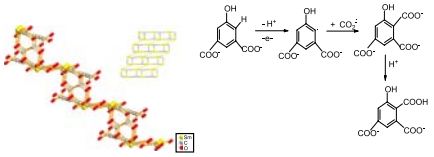

Hydrothermal reactions of $Sm(NO_3)_3 \cdot 6H_2O$ or $SmCl_3 \cdot 6H_2O$ with 5-hydroxyisophthalic acid ($H_2$hisp) have given rise to two different kinds of Sm(III) coordination polymers. Single-crystal X-ray analyses reveal that compound **1** features a novel 2D stair-like structure with oxalate and a new organic ligand, 6-hydroxy-1,2,4-benzenetricarboxylate, while compound **2** gives the normal product and displays a novel 2D layer structure. Oxalate ligands have been formed via the in-situ reductive coupling of $CO_2$ molecules released from the decomposition of 5-hydroxyisophthalate ligands with the reduction of $NO_3^-$ and the new organic ligands have been formed via the in-situ carboxylation under the presence of $NO_3^-$.

---

**Phase and valence transitions in $Ba_2LnSn_xSb_{1-x}O_{6-\delta}$ ($Ln$ = Pr and Tb)**
Paul J. Saines, Brendan J. Kennedy, Margaret M. Elcombe, Hugh H. Harris, Ling-Yun Jang and Zhaoming Zhang
***Page 2941***

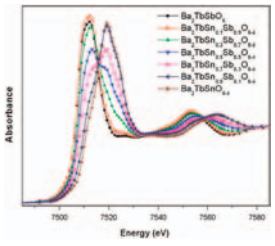


Powder diffraction and spectroscopic techniques have been used to investigate the series $Ba_2LnSn_xSb_{1-x}O_{6-\delta}$ ($Ln$ = Pr or Tb). It was found that increased $Sn^{4+}$ doping leads to oxidation of the $Ln^{3+}$ cations to $Ln^{4+}$. The X-ray absorption near-edge structure of the *Ln* $L_{III}$-edge indicates that this oxidation state change occurs gradually such that there are few oxygen vacancies present.

**Effect of the rare earth in the perovskite-type mixed oxides $A$MnO$_3$ ($A$ = Y, La, Pr, Sm, Dy) as catalysts in methanol oxidation**

B. Levasseur and S. Kaliaguine

***Page 2953***

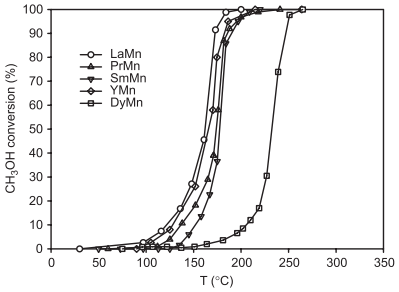


Perovskite-type mixed oxides $A$MnO$_3$ (with $A$ = Y, La, Pr, Sm, Dy) with high specific surface area were prepared by reactive grinding. The influence of the rare earth on the two kinds of oxygen in the perovskite structure ($\alpha$-O$_2$ and $\beta$-O$_2$) was correlated with a variety of intrinsic properties of the $A$-site cation. Moreover, the catalytic performance of the samples for methanol oxidation was evaluated.

---

**On the system cerium–platinum–silicon**

Alexander Gribanov, Andriy Grytsiv, Esmaeil Royanian, Peter Rogl, Ernst Bauer, Gerald Giester and Yurii Seropegin

***Page 2964***

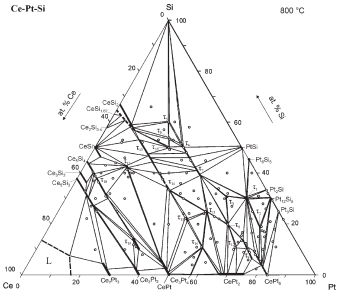


Phase relations in the ternary system Ce–Pt–Si have been established for the isothermal section at 800 °C based on X-ray powder diffraction, metallography, SEM and EMPA techniques on about 120 alloys. Nineteen ternary compounds were observed.

---

**Crystal structure of La$_{0.4}$Sr$_{0.6}$CoO$_{2.71}$ investigated by TEM and XRD**

C. Gspan, W. Grogger, B. Bitschnau, E. Bucher, W. Sitte and F. Hofer

***Page 2976***

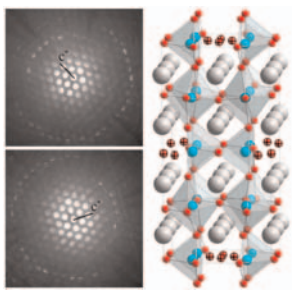

Two adjacent domains show different orientation of the $c$-axis of the tetragonal unit cell in the according convergent beam electron diffraction patterns.

**High-pressure high-temperature behavior of nitrogen-doped zirconia**

T. Locherer, D. Frost and H. Fuess

***Page 2983***

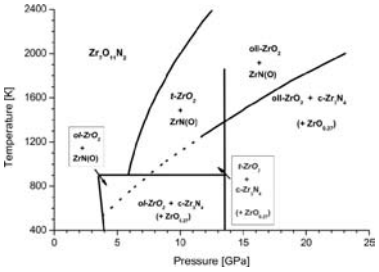


Draft for the decomposition reaction phase diagram of $Zr_7O_{11}N_2$ according to theoretical and experimental results.

---

**Interatomic versus intraatomic Ru interactions in perovskites**

Sangwon Kim, Ronald I. Dass and John B. Goodenough

***Page 2989***

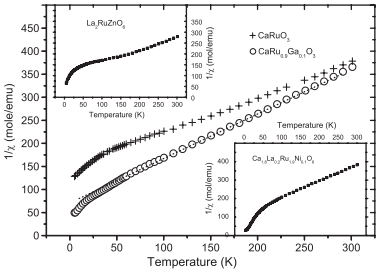


The competition between interatomic Ru–O–Ru interactions responsible for itinerant-electron ferromagnetism in SrRuO$_3$ and intraatomic spin–orbit coupling that suppresses some Ru–O–Ru magnetic interactions in CaRuO$_3$ so as to prevent long-range magnetic order has been further tested by investigating the double perovskites La$_2$RuZnO$_6$, La$_2$RuCoO$_6$, La$_2$TiCoO$_6$, and the solid solution Ca$_{2-2x}$La$_{2x}$Ru$_{2-x}$Co$_x$O$_6$ ($0.0 \leqslant x \leqslant 1.0$).

---

**Phase and valence transitions in Ba$_2$*Ln*Sn$_x$Nb$_{1-x}$O$_{6-\delta}$**

Paul J. Saines, Brendan J. Kennedy, Bernt Johannessen and Sarah Poulton

***Page 2994***

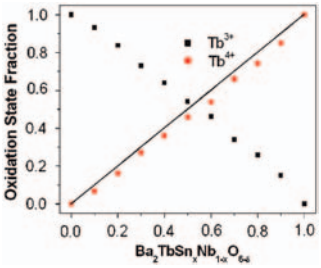


The series Ba$_2$*Ln*Sn$_x$Nb$_{1-x}$O$_{6-\delta}$ (*Ln* = Pr and Tb) has been investigated using powder diffraction and spectroscopic techniques. Similarly to the analogous $Sb^{5+}$ containing compounds it was found that $Sn^{4+}$ doping leads to the gradual oxidation of the $Ln^{3+}$ cations to the $Ln^{4+}$ state. Quantitative analysis of the *Ln* $L_{III}$-edge absorption spectra indicates that few or no oxygen vacancies are present.

*Continued*

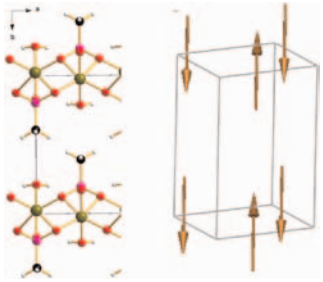

Crystal structure and magnetic structure of $Fe[(CD_3PO_3)(D_2O)]$.



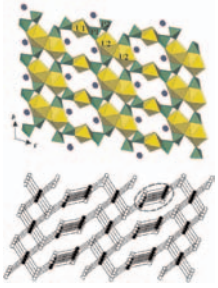

Polyhedral and topological presentation of $Li_2[(UO_2)_3(P_2O_7)_2]$ crystal structure.



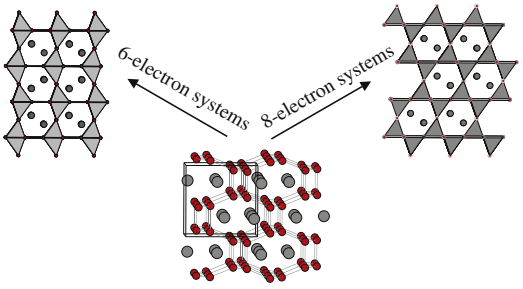


$CeCu_2$-type polar intermetallics can be transformed to Laves phases upon simultaneous application of pressure and temperature. The observed structures are controlled by the valence electron concentration.



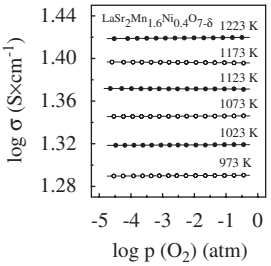


The substitution of manganese with nickel in Ruddlesden–Popper-type $LaSr_2Mn_2O_{7-\delta}$, where the solubility limit corresponds to approximately 25% Mn sites, increases phase stability at elevated temperatures and thermal expansion, and decreases unit cell volume and total conductivity. The Seebeck coefficient and conductivity of $LaSr_2Mn_{1.6}Ni_{0.4}O_{7-\delta}$, analyzed in the oxygen partial pressure range $10^{-15}$–0.3 atm at 600–1270 K, display that the electronic transport is n-type and occurs via a small polaron mechanism.



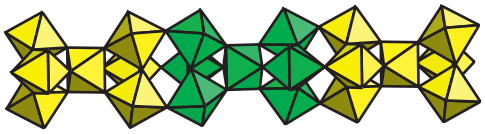

A unique chain-structure vanadium(III) fluoride $[C_4H_{12}N_2]_3[V_7F_{27}]$, based on a pyrochlore-like building unit, has been prepared solvothermally. Despite antiferromagnetic interactions, no long-range magnetic order occurs above 2 K, suggesting possible frustration.



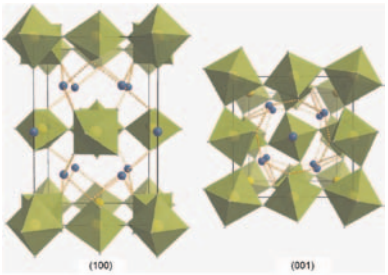


Projections of the $Na_5Al_3H_{14}$ structure. Na atoms are represented by small spheres. The polyhedra represents the $AlH_6$ moiety.

**A simple aqueous metathesis reaction yields new lanthanide monothiophosphates**

Nathan J. Takas, Lauren E. Slomka, Xiaocheng Yang, Nancy Giles and Jennifer A. Aitken

***Page 3044***

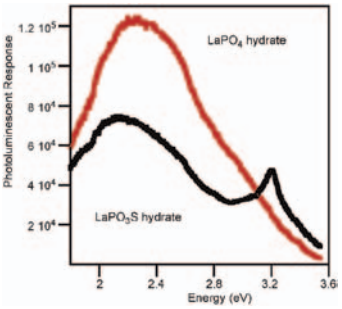


This paper describes the synthesis and characterization of two, new rare earth monothiophosphate materials, $LaPO_3S \cdot xH_2O$ and $NdPO_3S \cdot yH_2O$. Each of these was found to exist in a phase similar to the orthophosphate mineral, rhabdophane. The monothiophosphate hydrates displayed broad photoluminescence in the visible under excitation by a 325 nm laser.

---

**Structural and magnetic characterisation of Aurivillius material $Bi_2Sr_2Nb_{2.5}Fe_{0.5}O_{12}$**

E.E. McCabe and C. Greaves

***Page 3051***

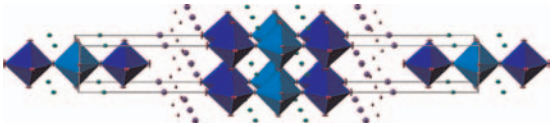

We report here the synthesis and characterisation of the Aurivillius material $Bi_2Sr_2Nb_{2.5}Fe_{0.5}O_{12}$. Combined Rietveld refinements using NPD and XRPD data have been used to investigate the structure and suggest that the material shows significant cation ordering as well as some local structural distortions. $Bi_2Sr_2Nb_{2.5}Fe_{0.5}O_{12}$ is paramagnetic in the temperature range studied.

---

**Crystallographic and infrared spectroscopic study of bond distances in $Ln[Fe(CN)_6] \cdot 4H_2O$ ($Ln$ = lanthanide)**

Xianju Zhou, Wing-Tak Wong, Michèle D. Faucher and Peter A. Tanner

***Page 3057***

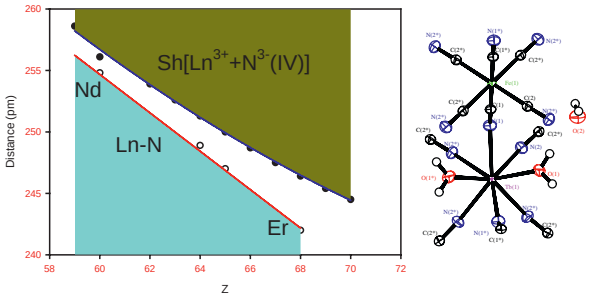


Crystallographic and FTIR data for $Ln[Fe(CN)_6] \cdot 4H_2O$ enable the changes in $Ln$–O, $Ln$–N, C≡N and Fe–C distances to be determined and modeled across the lanthanide series.

**High-throughput and microwave investigation of rare earth phosphonatoethanesulfonates—$Ln(O_3P–C_2H_4–SO_3)$ ($Ln$ = Ho, Er, Tm, Yb, Lu, Y)**

Andreas Sonnauer and Norbert Stock

***Page 3065***

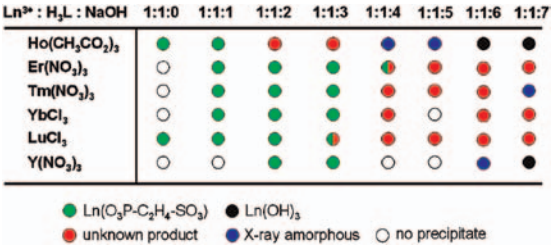


A high-throughput and microwave investigation of the System $LnX_3/H_2O_3P–C_2H_4–SO_3/NaOH/H_2O$ led to six new compounds $Ln(O_3P–C_2H_4–SO_3)$ with $Ln$ = Ho, Er, Tm, Yb, Lu, Y.

---

**The first di-cadmium-substituted vanadoarsenate derived from α-$\{As_8V_{14}O_{42}\}$ shell**

Dan Zhao, Shou-Tian Zheng and Guo-Yu Yang

***Page 3071***

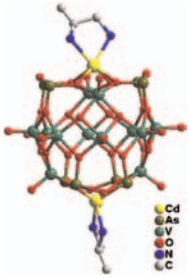


A new Cd-substituted vanadoarsenate $[Cd(enMe)_3]_2\{\alpha\text{-}[(enMe)_2Cd_2As_8V_{12}O_{40}(0.5H_2O)]\} \cdot 5.5H_2O$ was hydrothermally synthesized and characterized by EA, IR, TGA, UV–Vis, XRD, magnetic measurement and single crystal structural analysis. This compound exhibits the first di-Cd-substituted vanadoarsenate derived from α-$\{As_8V_{14}O_{42}\}$ shell.

---

**Structure and luminescence properties of silver-doped $NaY(PO_3)_4$ crystal**

M. El Masloumi, V. Jubera, S. Pechev, J.P. Chaminade, J.J. Videau, M. Mesnaoui, M. Maazaz and B. Moine

***Page 3078***

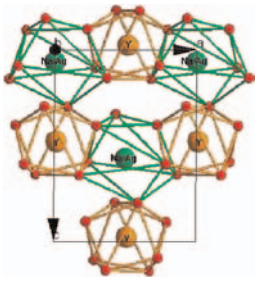

The presence of only one $Ag^+$ luminescence centre is the result from the perfect isolation ($Ag^+–Ag^+ = 5.90$ Å) of each oxygenated silver site ($AgO_8$ polyhedra) sharing two faces and one corner with three yttrium polyhedra.

*Continued*

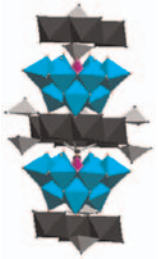

Optimum conditions for intercalation of Keggin-type anions in Ni, Zn hydroxysalts have been identified. Lacunary species are formed via partial depolymerization of the starting anion. The thermal decomposition of the intercalated phases has been also studied.



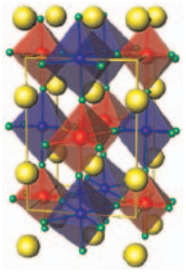

La-doped $Sr_2CoWO_6$ double perovskites have been prepared in polycrystalline form by solid-state reaction. The general formula of these compounds is $Sr_{2-x}La_xCoW_{1-y}Co_yO_6$ ($y = x/4$). XRPD, NPD and magnetic susceptibility studies were performed. The structure of monoclinic La-doped phases contains alternating $CoO_6$ and $(Co/W)O_6$ octahedra, almost fully ordered. NPD and magnetic measurements indicate an antiferromagnetic ordering at low temperature.



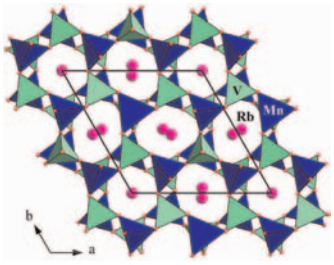


The new vanadates $AgMnVO_4$ and $RbMnVO_4$ have been synthesized by solid state reaction. They crystallize with a maricite-type and a stuffed tridymite-type structure, respectively. Antiferromagnetic interactions were observed in both compounds.



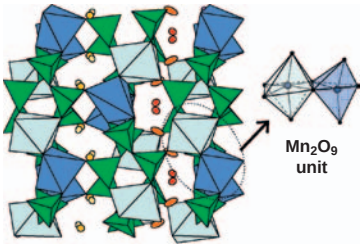


The 3D structure of $Li_2Mn^{II}P_2O_7$ (synthesized by solid-state reaction) is built from $P_2O_7$ diphosphate groups sharing corners with original $Mn_2O_9$ units. The lithium cations sit in the tunnels of the framework on four independent sites. Magnetic measurements have been performed, showing a paramagnetic behaviour. The relationships with the other compounds of the $A_2MP_2O_7$ series are analysed.



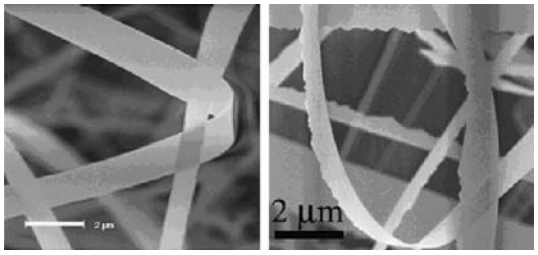


Millimeter-long single-crystalline ZnS nanobelts were grown on specific locations on a large scale. There are two kinds of nanobelts in the products—one has two smooth sides, and the other has one smooth side and one saw-teeth-like side, namely nanosaws. Mechanisms for the longitudinal direction growth of the nanobelts/nanosaws and the side saw-teeth direction growth of the nanosaws are discussed.



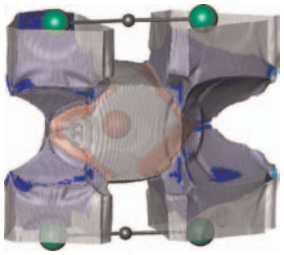

Polar multicenter Os–La bonding in the compound $La_7Os_4C_9$ is discussed in position space from a combined analysis of the electron localizability indicator (ELI-D) and the electron density. The picture shows five electron density basins (gray translucent) for atom types Os (green spheres) and La (red spheres) and only those parts (in blue colour) of 4 Os–La multicenter ELI-D basins, which are intersected by the electron density basins displayed.

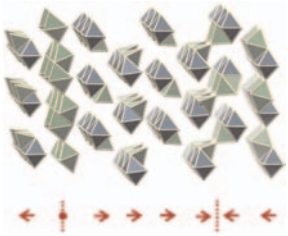

Chains of $[FeS_6]$-octahedra that are isotactically capped on one side by $[FeS_4]$-tetrahedra dominate the acentric structure. The unit cell contains two layered domains of opposite polarity with unbalanced size ratio. Vacancies in the iron sites follow a sinusoidal occupation modulation corresponding to a frozen charge-density wave.



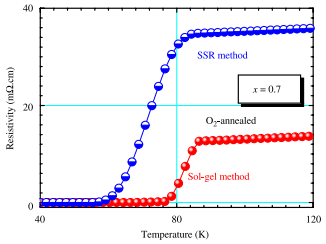


A series of Sr-based Hg-1212 superconducting cuprate $(Hg_{1-y}Se_y)Sr_2(Y_{1-x}Ca_x)Cu_2O_{6+\delta}$ have been synthesized using highly homogenous and reactive precursor $Sr_2(Y_{1-x}Ca_x)Cu_2O_z$ prepared by the citrate sol–gel process. The superconductor ceramics obtained from the sol–gel precursor was found to be so homogenous that the superconducting transition was steeper than the ceramic sample prepared by the solid-state reaction (SSR) method.



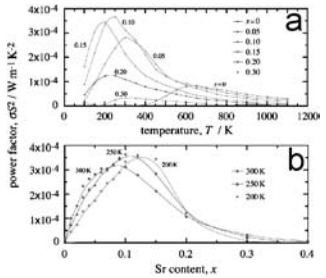


Temperature and Sr-doping level dependencies of the power factor of $La_{1-x}Sr_xCoO_3$.



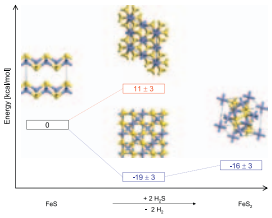


Reactions of mackinawite (FeS) with $H_2S$. In the absence of electron acceptors the system remains in the $Fe^{2+}/S^{2-}$ regime and endothermic pyrrhotite phases form (upper pathway). Only in the presence of electron acceptors, FeS phases with iron or sulfur in higher oxidation states can form and FeS reacts under these conditions exothermic to pyrite ($FeS_2$) via greigite ($Fe_3S_4$) as intermediate (lower pathway).



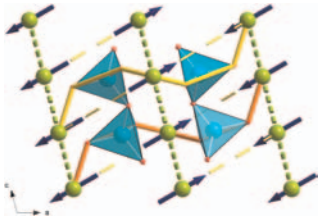

The magnetic properties and magnetic spins structures of 4 members of the clinopyroxenes are determined from susceptibility measurements and neutron diffraction. The magnetic ordering is accompanied by distinct alterations in structural parameters such as unit cell dimensions and interatomic distances.



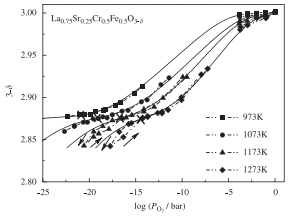


Oxygen nonstoichiometry of $(La_{0.75}Sr_{0.25})(Cr_{0.5}Fe_{0.5})O_{3-\delta}$ was plotted as the functions of partial oxygen pressure and temperature. The results were well explained by the localized electron on the Fe-sites and the equilibrium constants of the defect chemical equation were determined. A hysteresis was observed under the reducing atmospheres above 1173 K due to decomposition of Fe ions.

*Continued*

## *Note*

**A new 3D nickel(II) framework composed of large rings: Ionothermal synthesis and crystal structure**

Ling Xu, Eun-Young Choi and Young-Uk Kwon

***Page 3185***

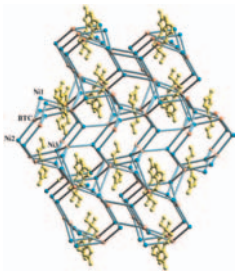

A novel 3D framework $[AMI][Ni_3(BTC)_2(OAc)(MI)_3]$ is obtained in ionothermal system with $[AMI]^+$ incorporating in the cavities as structure directing template and $BTC^{3-}$ showing a new coordination fashion. The 3D framework is constructed by 2D layers linked with 1D double chains. The title compound has the middle thermal stability at ca. 280 °C.